Ductile fracture of bulk metallic glass $Zr_{50}Cu_{40}Al_{10}$ under high strain-rate loading

L. Lu [a,b,c], C. Li [c,e], W.H. Wang [d], M.H. Zhu [b], X.L. Gong [a,*], S.N. Luo [b,c,**]

[a] CAS Key Laboratory of Mechanical Behavior and Design of Materials, Department of Modern Mechanics, University of Science and Technology of China, Hefei, Anhui 230027, PR China
[b] Key Laboratory of Advanced Technologies of Materials, Ministry of Education, Southwest Jiaotong University, Chengdu, Sichuan 610031, PR China
[c] The Peac Institute of Multiscale Sciences, Chengdu, Sichuan 610207, PR China
[e] College of Physical Science and Technology, Sichuan University, Chengdu, Sichuan 610064, PR China
[d] Institute of Physics, Chinese Academy of Science, Beijing 100190, PR China

ARTICLE INFO

ABSTRACT

We investigate dynamic fracture or spallation of a ternary bulk metallic glass, $Zr_{50}Cu_{40}Al_{10}$, under high strain-rate (4–5×10^5 s^{-1}) loading. Both incipient and full spall are achieved. Free-surface velocity histories and microstructure features of the recovered samples, such as necking, softening, microvoids, and rounded cups/cones, indicate exceptional ductility in deformation and fracture of this glass. Softening/necking is attributed to decreased glass transition temperature with increasing tension, and rounded cups/cones, to localized shear banding, void formation, and their interactions.

© 2015 Elsevier B.V. All rights reserved.

1. Introduction

Bulk metallic glasses (BMGs), also referred to as bulk amorphous metals, differ from general metals in their disordered atomic structures and multicomponent metal alloy systems, and exhibit excellent mechanical properties, such as large elastic strain and high yield strength [1–4], while their low ductility is still a concern. Copious studies have investigated their responses to loading at various strain rates, such as quasi-static or Hopkinson bar compression/tension, and planar impact. Ductile deformation and fracture under high strain-rate loading are relatively under-explored and of particular interest. Recently, macroscopic and nanoscale or atomic ductility were observed in quasi-static experiments [5–12]. In addition, high strain-rate spallation experiments were conducted to investigate Hugoniot elastic limit (HEL), spall strength, and fracture mechanisms of BMGs, mostly quinary or senary BMGs [13–17]. Such BMGs show certain ductility under high strain-rate loading, but higher ductility is desirable. In this work, we explore high strain-rate deformation and fracture of a

ternary BMG, $Zr_{50}Cu_{40}Al_{10}$, with gas-gun plate impact loading and laser-velocimetry measurements. The shock-recovered samples are examined with scanning electron microscope (SEM). Both incipient and full spallation are observed. Free-surface velocity histories and microstructure features of the recovered samples, such as necking, softening, microvoids, and rounded cups/cones, indicate its exceptional ductility as a BMG. Deformation mechanisms are proposed to explain the observations.

2. Materials and experiments

A Zr-based BMG ingot, $Zr_{50}Cu_{40}Al_{10}$, is prepared by arc-melting mixtures of pure Zr, Cu and Al in an argon atmosphere, and then remelted and cast into a copper mold to obtain a cylindrical rod with a diameter of 10 mm. The rod is sectioned into multiple samples. The samples are disks with a diameter of 10 mm and a thickness of 1 mm. At ambient conditions, the density is measured by an Archimedean method to be $\rho_0 = 6.94$ g cm^{-3}, the longitudinal sound speed determined from ultrasonic measurements is $C_L = 4.74$ km s^{-1}, Poisson's ratio is $\nu = 0.37$ [18,19], and then the bulk sound speed is obtained as $C_0 = 4.04$ km s^{-1}. The flyer plates with a 0.41-mm thickness are made of high-purity Cu, with $\rho_0 = 8.95$ g cm^{-3} and $C_0 = 3.94$ km s^{-1}. Two parallel surfaces of a sample or flyer plate disk are polished to micron level or mirror

* Corresponding author.
** Corresponding author at: The Peac Institute of Multiscale Sciences, Chengdu, Sichuan 610207, PR China.
E-mail addresses: gongxl@ustc.edu.cn (X.L. Gong), sluo@pims.ac.cn, sluo@swjtu.cn (S.N. Luo).
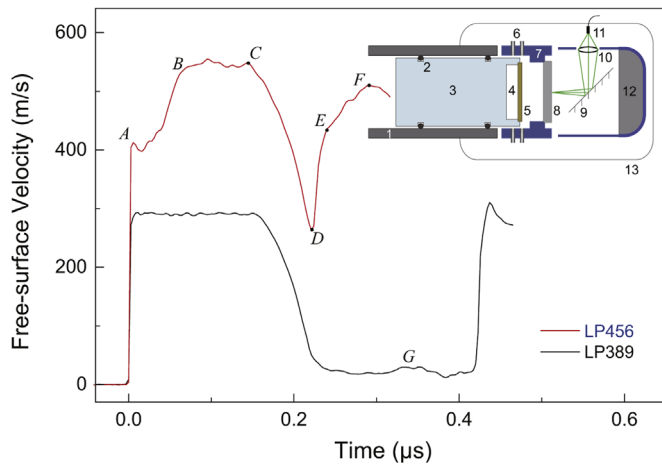
Fig. 1. Representative free-surface velocity–time histories of $Zr_{50}Cu_{40}Al_{10}$ BMGs under planar impact. Inset: Schematic setup for gas-gun plate-impact spallation experiments. 1: gun barrel; 2: O-ring; 3: polycarbonate sabot; 4: recess for release waves; 5: flyer plate; 6: optical fibers and detectors for the optical beam block system; 7: sample holder; 8: sample; 9: mirror; 10: lens; 11: optical fiber connected to Doppler pin system (DPS); 12: soft materials; 13: vacuum chamber.

finish.

For high strain-rate loading, flyer-plate impact experiments are conducted with a 10-mm bore, single-stage, tabletop gas gun to investigate dynamic compression and tension responses of the BMG samples. The methodology as well as data analysis related to planar impact experiments can be found in other studies [20–23]. The inset in Fig. 1 shows the schematic setup of flyer-plate planar impact experiments. A flyer plate (5) is attached to polycarbonate sabot (3), with a recess (4) immediately behind it. When a solenoid valve is fired, compressed helium is released from a high-pressure gas reservoir into the gun barrel (1), accelerating the sabot and flyer plate assembly. Upon exiting the muzzle, the flyer plate impacts the target or sample (8) under consideration. The flyer plate velocity is measured with an optical beam block system (6), and the free surface velocity of the target, with a Doppler pin system or DPS (11). A single-mode optical fiber is used as the DPS probe and collects reflected light carrying velocity information. Superposition of the Doppler-shifted light reflected from a moving interface/free surface with the reference light reflected from a static surface create interference fringes, and the beat frequency is proportional to the interface/free surface velocity. Optical signals are analyzed to deduce velocity histories via fast Fourier transformation. The muzzle, target and diagnostics are located in a vacuum chamber (13). The shocked samples are "soft" recovered with foams (12) for SEM examination.

3. Results and discussion

Spallation experiments are conducted at four impact velocities, 283 m s^{-1}, 369 m s^{-1}, 449 m s^{-1}, and 534 m s^{-1}, corresponding to shots LP389, LP437, LP422, and LP456, respectively. Representative free-surface particle velocity (u_{fs}) profiles are shown in Fig. 1. With increasing impact velocity, this BMG exhibits a transition from incipient to full spallation. For the experiment conducted at the lowest impact velocity (LP389), a single elastic shock forms. At higher impact velocities, the free-surface velocity profiles show clearly an elastic–plastic (two-wave) structure, i.e., segments OA (elastic) and AB (plastic). Segment BC denotes the plastic shock plateau. The Hugoniot elastic limit, calculated by $\sigma_{HEL} = \frac{1}{2}\rho_0 C_L u_{fs}|_A$, is about 6.8 GPa. The yield stress σ_y is related to σ_{HEL} via $\sigma_y = \sigma_{HEL}(1 - 2\nu)/(1 - \nu)$, and $\sigma_y = 2.8$ GPa.

The arrival of the release fan reflected from the free surface of the flyer plate leads to velocity decrease (CD in Fig. 1). The interaction of this release fan with that initiated from the target plate free surface releases the mid-part of the sample from compression into tension. Once the tensile stress exceeds a critical stress, termed as the spall strength σ_{sp}, spall occurs and is demonstrated on u_{fs} as a re-acceleration (DF). The spall strength can be calculated as $\sigma_{sp} \approx \frac{1}{2}\rho_0 C_L \Delta u_{fs}$, here Δu_{fs} is the difference in u_{fs} between C and D (Fig. 1). The tensile strain rate can be estimated with $\dot{\varepsilon} \approx [du_{fs}(t)/dt]_{release}/(2C_0)$. The spall strengths are estimated to be 4.4, 4.1, 4.5, and 4.7 GPa, in the order of increasing impact velocity. The tensile strain rates are about $4–5 \times 10^5 \text{ s}^{-1}$. σ_{sp} for the incipient spall (LP389) shot is higher than the lowest full spallation shot (LP437), since the shock is purely elastic for the former and compression-induced damage is negligible. The re-acceleration is clearly composed of two stages, DE and EF, which represents growth and coalescence of isolated cracks or voids, respectively, and this feature is a characteristic of ductile fracture in general.

In order to investigate the microstructure of a shock-recovered sample, it is sectioned into two halves along the impact direction with a low-speed diamond saw, mechanically polished with 2000 grit silicon sand paper and 0.3 µm alumina particles. Fig. 2 shows SEM images of the cross-section of the shock-recovered sample (incipient spall, LP389). There is only a small crack, ~400 µm long, in the midsection [Fig. 2(a)]. Such incipient spall feature is consistent with the minor re-acceleration observed in the $u_{fs}(t)$ profile (G in Fig. 1). The crack shows a serrated profile rather than a straight line expected for brittle fracture, and certain regions of the crack remain partially connected [Fig. 2(b)]. We observe necking of the ligaments between neighboring voids [black arrows, Fig. 2 (c) and (d)]. The length of the ligaments is about 4–5 µm, and the narrowest width (w_n) is ~1 µm. We define the necking parameter as $\psi = (w_0 - w_n)/w_0 \times 100\%$, where w_0 is the original width. ψ is about 65%. During tension, microvoids randomly nucleate and grow, and the ligaments between neighboring microvoids undergo ductile deformation via necking. These features are typical of plastic deformation, and demonstrate that some amount of plasticity can occur at micron level in this BMG under high strain-rate loading.

In addition to plastic deformation, softening is also observed as nanocones oriented nearly perpendicular to the local crack surface [Fig. 2(e)], and ductile dimples distributed uniformly on the fracture surface [white arrow, Fig. 2(f)]. Upon dynamic tension, viscosity near the spall plane is reduced to a level comparable to that of a liquid, allowing for the formation of a cone. Different local viscosities lead to various morphologies; higher viscosity corresponds to ductile dimples associated with considerable plasticity, while the cone feature reflects a lower viscosity. Necking and softening clearly demonstrate remarkable microscale plasticity and viscous flow during gas gun loading.

Higher impact velocities (369, 449, and 534 m s^{-1}) induce full spall, and the samples break in half along the spall plane. Fig. 3 presents SEM micrographs of spall fracture surfaces. Two distinct structures are common on the fracture surfaces, i.e., cup and cones, as shown in Fig. 3(a) and (b), respectively. Their sizes range from 10 to 200 µm. The depth profiles (red curves) for cups or cones are plotted in Fig. 3(a), (b), (f) and (g). Fig. 3(c) and (d) shows two important cup structures, and both contain a core-like center and vein-like patterns. Ridgelines (marked with white arrows) appear as the boundaries of the cups under tension. Around the core-like centers, shear bands (marked with black arrows) extend and terminate at a microvoid [marked with a circle, Fig. 3(h)] or a melted region near a microvoid [Fig. 3(i)]. Molten droplets of various sizes are found around the microvoid. Moreover, microvoids and molten droplets [Fig. 3(j)] similar to those in Fig. 3(i) are
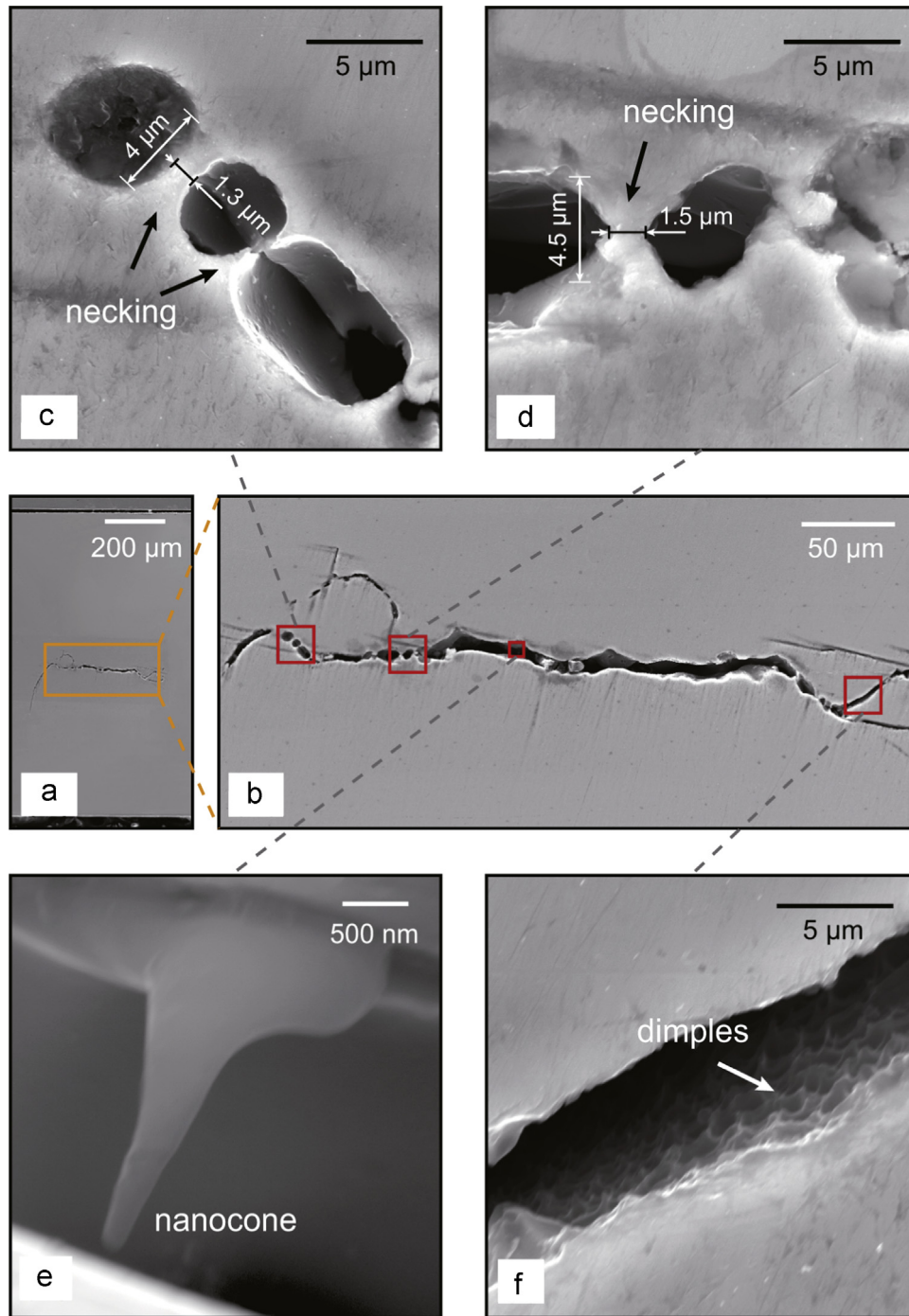
Fig. 2. (a) Cross-sectional SEM images of the shock-recovered BMG for an impact velocity of 283 m s^{-1}. (b)–(f) are magnified images corresponding to the regions indicated by the rectangles.

also observed on the top of cones. Therefore, a microvoid connects a cup and a cone located at the same position of two halves before separation. Both incipient and full spall show decreased viscosities and micro features of ductile deformation, but the latter shows richer microstructure features including cup/cone structures, shear bands and microvoids.

BMGs possess the characteristics of both metals and glasses. Their glass transformation temperatures (T_g) increase with increasing pressure [24], similar to high pressure melting curves of normal solids. When the stress state transits from compression to tension, T_g decreases accordingly, lower than the local temperature

on the spall plane T_{sp} [21]. Possible mechanisms of necking and softening as observed in the incipient spall experiment are proposed in Fig. 4(a). When T_g is higher than T_{sp}, a sample undergoes brittle failure, while ductile deformation occurs if T_g is below T_{sp}. When the stress is further reduced, viscous flow is induced. Consistently, brittle deformation transits to plastic deformation under quasi-static tensile loading via increasing temperature, and the apparent macroscopic flow experiences a change from non-Newtonian to Newtonian flows when temperature exceeds T_g [25].

Fracture is accompanied by the appearance of the cup/cone structures and microvoids, and the mechanism is shown
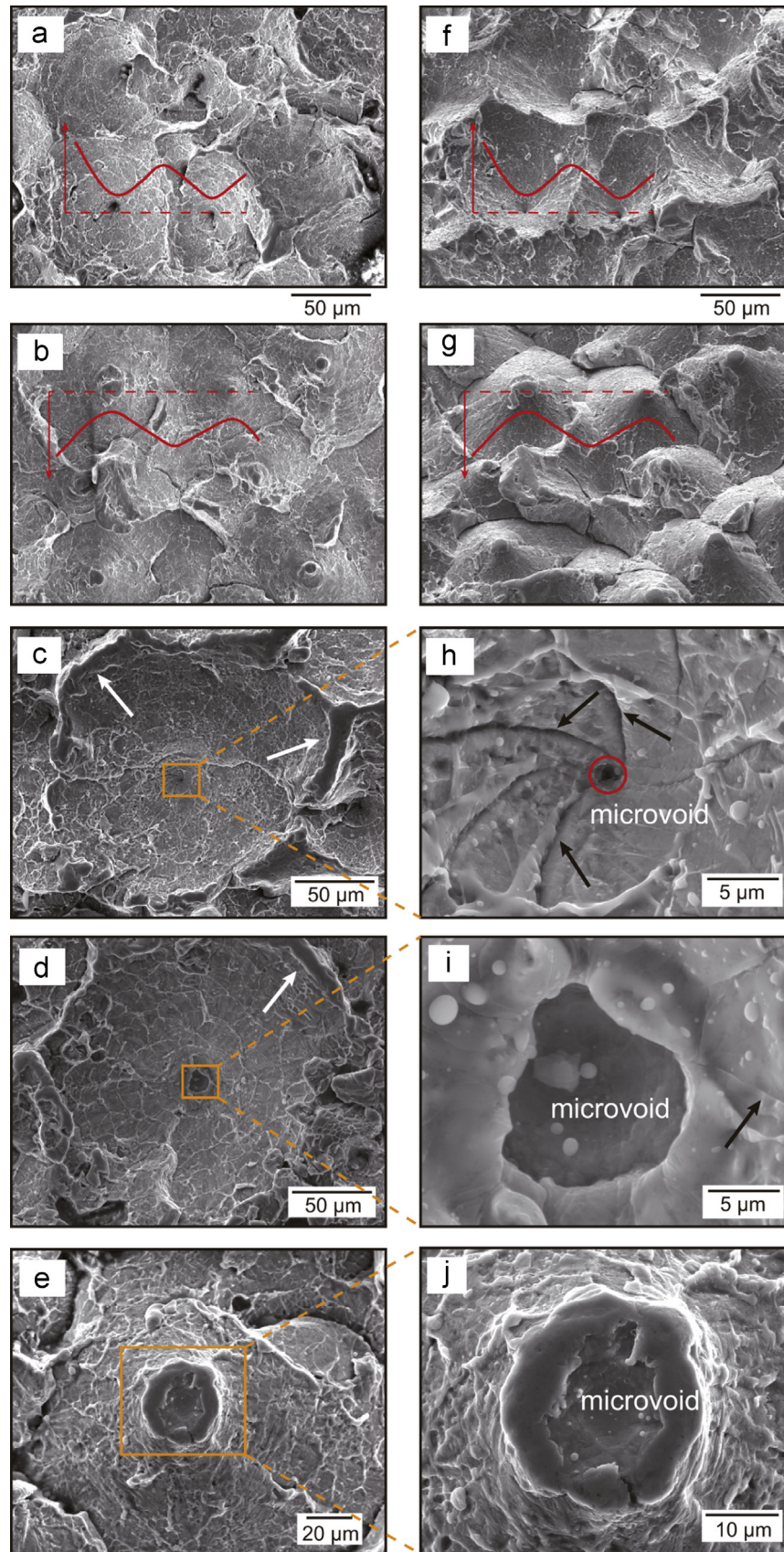
Fig. 3. Spall fracture surfaces characteristics of the shock-recovered BMGs. For (a)–(c) and (e), the impact velocity is 369 m s^{-1}, while it is 449 m s^{-1} for (d). (a) and (f), (b) and (g) represent different views of the same regions. (h)–(j) are magnified images corresponding to the regions indicated by rectangles. The solid curves in (a), (b), (f) and (g) depict schematically the height profiles along the dashed lines. (For interpretation of the references to color in this figure, the reader is referred to the web version of this paper.)
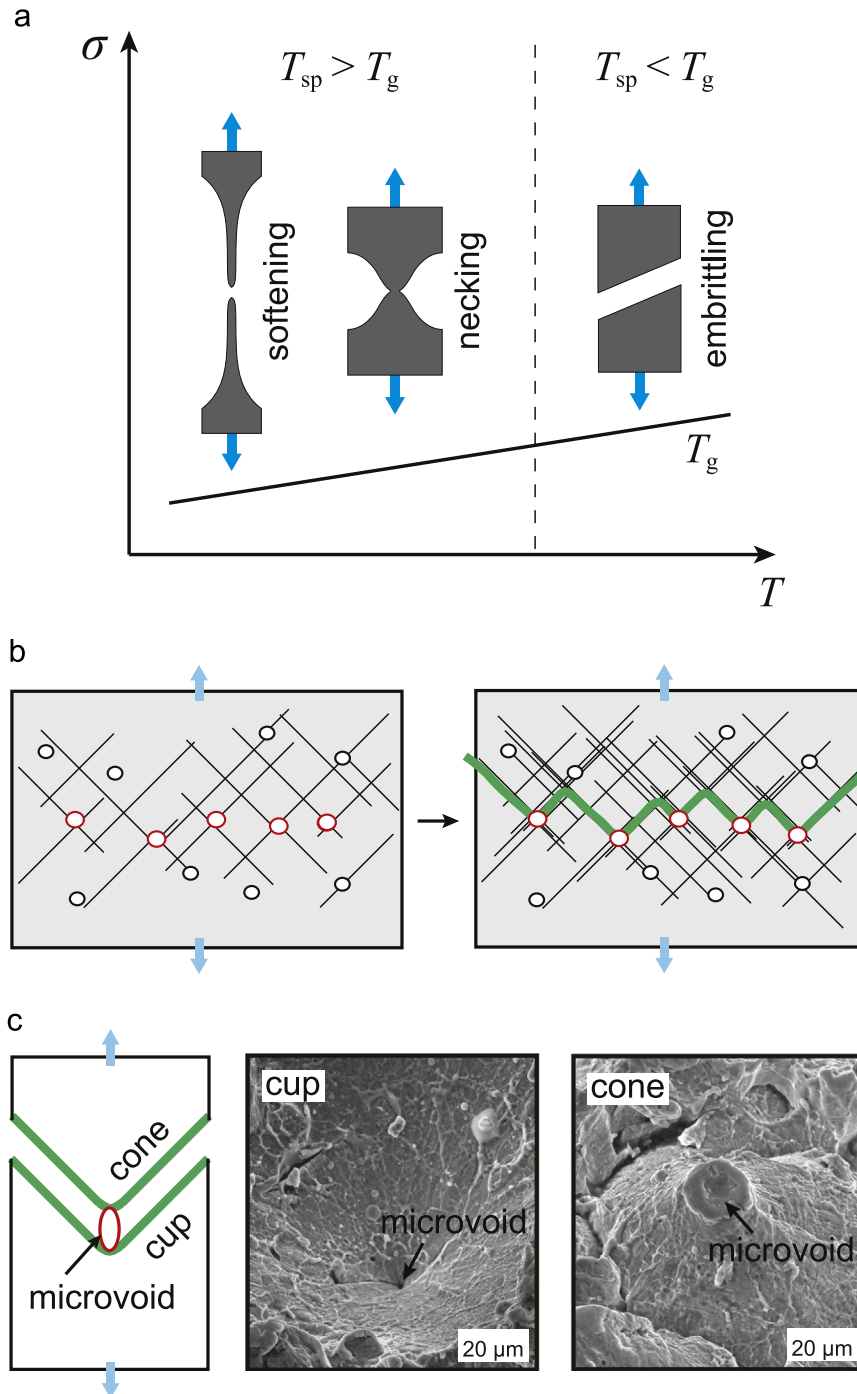
Fig. 4. (a) Schematic stress–glass transition temperature plot, and illustrations of brittle, ductile, and softening fracture modes. (b) Schematic drawings of microstructure features related to spallation. (c) Schematics of a cup–cone pair and a microvoid located between, along with illustrative SEM micrographs. In (a), σ: stress; T_g: glass transition temperature; T_{sp}: temperature at the spall plane prior to fracture. In (b), green curves: fracture surface formed by shear deformation zones and softened regions (red circles); black lines: shear deformation zones; black circles: free volume. (For interpretation of the references to color in this figure caption, the reader is referred to the web version of this paper.)

schematically in Fig. 4(b). Compression or tension induce shearing, and shear transformation zones and "shear bands" (black lines) are activated. Microvoids (red circles) nucleate at the intersections of shear deformation zones or shear bands, the weakest spots [26], or in free volumes [16], as a result of ductile deformation under tension. Microvoids grow under tension, and the regions around them show viscous feature. The shear deformation zones are weak spots as well, where fracture occurs, and a cup and a cone form during separation (Fig. 4(c)). The shear deformation zones are connected to form a spall "plane." During the separation, a microvoid is severed as well, with one-half located at the top tip of the cone, and another half, at the bottom tip of the cup, as shown by the schematic and SEM micrographs in Fig. 4(c).

Nanowires of another ternary metallic glass, $Al_{90}Fe_5Ce_5$, were elongated from 9 to 31 nm with a 70% width reduction during quasi-static tension [11]. Under planar impact, $Zr_{50}Cu_{40}Al_{10}$ BMG can be elongated to 4–5 μm with a width reduction of 65%, while most quinary or senary BMGs show low ductility. Therefore, this ternary BMG $Zr_{50}Cu_{40}Al_{10}$ appears to excel in ductility under high strain-rate tensile loading among those glasses examined.

4. Conclusions

In summary, planar impact experiments are conducted to investigate dynamic fracture of a ternary BMG, $Zr_{50}Cu_{40}Al_{10}$. HEL and yield stress are determined as 6.8 GPa and 2.8 GPa, respectively. At impact velocities of 282–534 m s^{-1} (Cu flyer plates), incipient and full spall are observed at a spall strength of 4–5 GPa. The two segments of re-acceleration (induced by spall) on the free-surface velocity histories, and microstructure features such as necking, elongation, ductile dimples, molten droplets and cups/cones, demonstrate distinct ductile and softening deformation under high strain-rate tension. Softening/necking is attributed to decreased glass transition temperature with increasing tension, and rounded cups/cones, to localized shear banding, void formation, and their interactions.

Acknowledgments

References

[1] A.L. Greer, Science 267 (1995) 1947.
[2] W.H. Wang, C. Dong, C.H. Shek, Mater. Sci. Eng. R 44 (2004) 45.
[3] M.W. Chen, Annu. Rev. Mater. Res. 38 (2008) 445.
[4] B.A. Sun, W.H. Wang, Prog. Mater. Sci. 74 (2015) 211–307.
[5] C.C. Hays, C.P. Kim, W.L. Johnson, Phys. Rev. Lett. 84 (2000) 2901.
[6] J. Schroers, W.L. Johnson, Phys. Rev. Lett. 93 (2004) 255506.
[7] J. Das, M.B. Tang, K.B. Kim, T. Theissmann, F. Baier, W.H. Wang, J. Eckert, Phys. Rev. Lett. 94 (2005) 205501.
[8] Y.H. Liu, G. Wang, R.J. Wang, D.Q. Zhao, M.X. Pan, W.H. Wang, Science 315 (2007) 1385–1388.
[9] H. Guo, P.F. Yan, Y.B. Wang, J. Tan, Z.F. Zhang, M.L. Sui, E. Ma, Nat. Mater. 6 (2007) 735–739.
[10] D.C. Hofmann, J.Y. Suh, A. Wiest, G. Duan, M.L. Lind, M.D. Demetriou, W.L. Johnson, Nature 451 (2008) 1085–1089.
[11] J.H. Luo, F.F. Wu, J.Y. Huang, J.Q. Wang, S.X. Mao, Phys. Rev. Lett. 104 (2010) 215503.
[12] J. Yi, W.H. Wang, J.J. Lewandowski, Acta Mater. 87 (2015) 1–7.
[13] S. Zhuang, J. Lu, G. Ravichandran, Appl. Phys. Lett. 80 (2002) 4522–4524.
[14] S.J. Turneaure, J.M. Winey, Y.M. Gupta, J. Appl. Phys. 100 (2006) 063522.
[15] F.P. Yuan, V. Prakash, J.J. Lewandowski, J. Mater. Res. 22 (2007) 402–411.
[16] J.P. Escobedo, Y.M. Gupta, J. Appl. Phys. 107 (2010) 123502.
[17] B.P. Wang, L. Wang, S. Wang, Q.B. Fan, Y.F. Xue, H.F. Zhang, H.M. Fu, Intermetallics 63 (2015) 12–18.
[18] Z.Y. Zhang, V. Keppens, P.K. Liaw, Y. Yokoyama, A. Inoue, J. Mater. Res. 22 (2007) 364–367.
[19] Z.Y. Zhang, V. Keppens, T. Egami, J. Appl. Phys. 102 (2007) 123508.
[20] M.A. Meyers, Dynamic Behavior of Materials, John Wiley & Sons, New York, 1994.
[21] S.N. Luo, Q. An, T.C. Germann, L.B. Han, J. Appl. Phys. 106 (2009) 013502.
[22] B.X. Bie, J.H. Han, L. Lu, X.M. Zhou, M.L. Qi, Z. Zhang, S.N. Luo, Compos. Part A: Appl. Sci. 68 (2015) 282–288.
[23] T. Li, D. Fan, L. Lu, J.Y. Huang, J.C. E, F. Zhao, M.L. Qi, T. Sun, K. Fezzaa, X.H. Xiao, X.M. Zhou, T. Suo, W. Chen, Y.L. Li, M.H. Zhu, S.N. Luo, Carbon 91 (2015) 468–478.
[24] J.Z. Jiang, W. Roseker, M. Sikorski, Q.P. Cao, F. Xu, Appl. Phys. Lett. 84 (2004) 1871–1873.
[25] Z. Wang, B.A. Sun, H.Y. Bai, W.H. Wang, Nat. Commun. 5 (2014) 5823.
[26] B. Arman, S.N. Luo, T.C. Germann, T. Çağın, Phys. Rev. B 81 (2010) 144201.